ACS NANO
Cite This: ACS Nano 2017, 11, 9914-9919
www.acsnano.org

ARTICLE

High Velocity Saturation in Graphene Encapsulated by Hexagonal Boron Nitride

Megan A. Yamoah,[†,‡] Wenmin Yang,[†,§] Eric Pop,[∥,⊥,#] and David Goldhaber-Gordon*[,†]

[†]Department of Physics, [∥]Department of Electrical Engineering, [⊥]Department of Materials Science & Engineering, and [#]Precourt Institute for Energy, Stanford University, Stanford, California 94305, United States

[‡]Department of Physics, Massachusetts Institute of Technology, Cambridge, Massachusetts 02139, United States

[§]Beijing National Laboratory for Condensed Matter Physics, Institute of Physics, Chinese Academy of Sciences, Beijing 100190, China

Supporting Information

ABSTRACT: We measure drift velocity in monolayer graphene encapsulated by hexagonal boron nitride (hBN), probing its dependence on carrier density and temperature. Due to the high mobility (>5 × 10^4 $cm^2/V/s$) of our samples, the drift velocity begins to saturate at low electric fields (~0.1 V/μm) at room temperature. Comparing results to a canonical drift velocity model, we extract room-temperature electron saturation velocities ranging from 6 × 10^7 cm/s at a low carrier density of 8 × 10^{11} cm^{-2} to 2.7 × 10^7 cm/s at a higher density of 4.4 × 10^{12} cm^{-2}. Such drift velocities are much higher than those in silicon (~10^7 cm/s) and in graphene on SiO_2, likely due to reduced carrier scattering with surface optical phonons whose energy in hBN (>100 meV) is higher than that in other substrates.

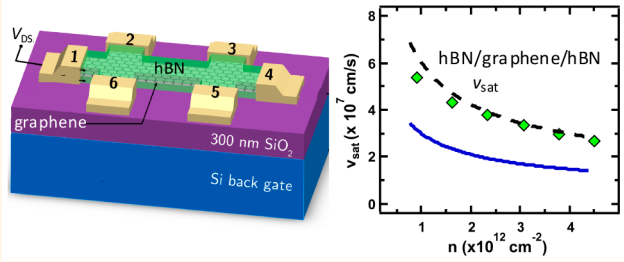

KEYWORDS: *graphene, boron nitride, drift velocity saturation, high field, phonon scattering*

Graphene-based electronic devices have been extensively investigated,[1−10] inspired by the material's unusual band structure,[11] high intrinsic mobility,[12] high thermal conductivity,[9,13] and ability to withstand high current densities.[14] Electron flow in graphene under low (lateral) electric fields shows distinctive behavior such as Klein tunneling[15] and the half-integer quantum Hall effect.[16] At low field, the electron or hole drift velocity is simply proportional to the electric field magnitude, through the mobility. In contrast, under high electric field, the drift velocity approaches a constant saturation velocity, v_{sat}, at which the rate of energy gain from the electric field is balanced by the rate of energy loss *via* inelastic phonon emission.[17,18] Transport under high electric fields should enable probing the electron− or hole−phonon interaction and could depend on high-energy details of the band structure. High saturation velocity is also vital for practical applications of graphene in radio frequency amplifiers[19] and high-current graphene interconnects.[14,20] For example, the intrinsic transit frequency of a transistor is limited by the saturation velocity: $f_T \approx v_{sat}/(2\pi L)$, where L is the channel length.

Due to graphene's atomically thin nature, the saturation velocity can be limited by both intrinsic graphene phonons and remote substrate phonons,[21,22,39] with lattice heating[4,8−10] and interfacial charged impurities also playing a role.[4,8,10] Reported room-temperature saturation velocities in graphene in contact with hBN and SiO_2 substrates, and on a SiO_2 substrate with an additional Al_2O_3 top gate dielectric are 2 × 10^7,[23] 1.9 × 10^7,[4] and 10^7 cm/s,[24] respectively, at a common carrier density of 5.0 × 10^{12} cm^{-2}. Encouragingly, velocities approaching the Fermi velocity of ~10^8 cm/s in graphene have been estimated in suspended samples[5] or by applying rapid bias pulses,[21] but these approaches are not relevant for most circuit applications.

hBN is a good candidate substrate for enhancing graphene saturation velocity for multiple reasons: (i) Its surface optical phonon (OP) energy of ~102 meV compared to 59 meV in SiO_2[8] should suppress the phonon emission process which is most commonly thought to limit v_{sat}. (ii) The high thermal conductivity of hBN[25] may limit self-heating, further decreasing electron−phonon scattering.[10] (iii) Graphene on hBN has shown mobility[26] much higher than that on other substrates, due to reduced impurity scattering. (iv) The Fermi velocity (v_F) of graphene, known to be dependent on the substrate dielectric constant, has been measured to be nearly 1.5 × 10^8 cm/s in graphene on hBN;[27] this is comparable to the v_F on SiO_2 and greater than that on substrates with a higher dielectric constant such as SiC, Al_2O_3, and HfO_2. Theoretical modeling considering the effects of lattice heating and substrate

Received: June 2, 2017
Accepted: September 7, 2017
Published: September 7, 2017

DOI: 10.1021/acsnano.7b03878
ACS Nano 2017, 11, 9914−9919

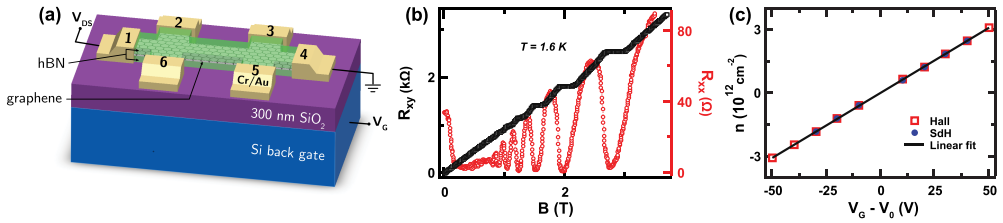

Figure 1. (a) Schematic of six-contact Hall bar on monolayer graphene device encapsulated by hBN. Data in main text are presented from a device with 2 μm channel width and 4 μm center-to-center separation between voltage probes. (b) Hall effect and longitudinal resistance as a function of perpendicular magnetic field at 1.6 K ambient temperature. (c) Extracted carrier density as a function of gate voltage, showing consistent results between Hall effect and Shubnikov–de Haas (SdH) measurements.

impurities predicts velocity saturation at ~2.5 × 10^7 cm/s in graphene on hBN at fields beyond 1 V/μm.[10] The same model predicts lower velocities of 2 × 10^7 and 1.5 × 10^7 cm/s on Al_2O_3 and HfO_2, respectively.

Despite these earlier studies, there are so far no direct measurements of graphene saturation velocity in samples *encapsulated* by hBN, which ought to provide nearly the best of all possible scenarios discussed earlier, including best heat spreading, lowest impurity density, and highest phonon energy, though the Fermi velocity may be slightly lower than that in samples with no top dielectric.

RESULTS AND DISCUSSION

Here, we created hBN-encapsulated monolayer graphene samples with Cr/Au edge contacts to achieve ultraclean, high-mobility devices, as shown in Figure 1a and Figure S1 (see Methods and Supporting Information). We employed gated multi-terminal test structures to directly probe charge transport as a function of carrier density and lateral electric field within the graphene Hall bars. Data were collected at ambient temperatures between 2 and 300 K with carrier densities up to 4.4 × 10^{12} electrons/cm^2 and 4.2 × 10^{12} holes/cm^2. We observe that the drift velocity saturates at a density-dependent value between 2.7 × 10^7 and 6 × 10^7 cm/s at room temperature (RT), higher than that in previous reports for graphene on other substrates and nearly 1.5 times higher than that predicted by theoretical models for graphene on hBN for similar carrier densities.[10] (Note, however, that our graphene encapsulated in hBN has substantially higher mobility than that envisioned in those models.) The saturation velocity is nearly independent of temperature and likely limited primarily by emission of hBN surface OPs, whose energy (~102 meV) is far above the ambient thermal energy.

For this paper, we systematically studied two devices without applying biases high enough to cause irreversible changes in transport. Results from one of these devices are presented in the main text, and v_{sat} data from the other are included in the Supporting Information. In the process of learning the phenomenology of our high-field measurements, we fabricated and studied 12 additional devices and on 8 of them collected significant data before causing irreversible changes. All such data were broadly consistent with those featured in the main text.

Figure 1 b shows the typical low electric field transport properties of the graphene device in perpendicular magnetic fields with a 100 nA (17.9 Hz) AC current flowing from source to drain (contacts 1 to 4 in Figure 1a). Both the longitudinal resistance R_{xx} between contacts 2 and 3, and Hall resistance R_{xy} between contacts 2 and 6 were measured. R_{xx} is a strong function of back gate voltage (V_G) at zero magnetic field and 300 K. As shown in the inset of Figure 2a, with decreased temperature the resistance peak at the charge neutrality point

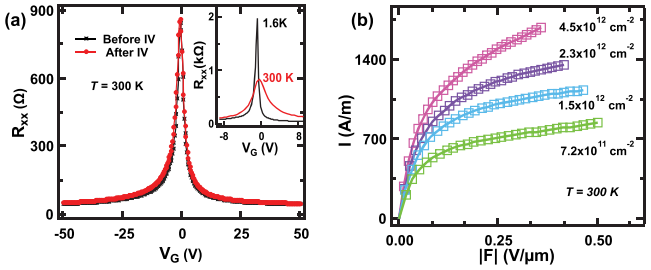

Figure 2. (a) Characteristic gate voltage sweep showing consistent R_{xx} curves before and after measurement. The charge neutrality point (CNP) occurs at $V_G = V_0 = -1$ V. The maximum resistance modulation (on/off) is ~18.5 at RT. Inset shows data at 300 and 1.6 K zoomed in near the CNP to better illustrate the temperature dependence of R_{xx}. (b) Measured current density *vs* field for various average carrier densities at RT.

(CNP) becomes higher and narrower due to suppression of thermally induced ambipolar conduction, and resistance at high density becomes lower due to reduced electron–phonon scattering. The resulting maximum resistance on/off ratio is ~18.5 at RT and ~445 at 1.6 K. At 1.6 K in a perpendicular magnetic field B, R_{xx} exhibits typical Shubnikov–de Haas (SdH) quantum oscillations equally spaced in B^{-1}, and R_{xy} is quantized at filling factors ν = 2, 6, 10, etc. (Figure 1b), as generally reported for high-mobility graphene devices.[28,29] Figure 1c displays the linear dependence of carrier density on gate voltage, and extraction from Hall effect or SdH oscillations gives mutually consistent results.

Current–voltage (I–V) measurements at high lateral electric fields were carried out in a four-terminal configuration to eliminate contributions from contact resistance. DC bias was applied between source and drain, and both current in the channel and four-terminal voltage between contacts 2 and 3 were measured (Figure 1a). We made most measurements with source–drain bias polarity (V_{DS}) chosen to increase rather than decrease carrier density for a given polarity of gate voltage (V_G). Care was taken to ensure all measurements were repeatable after high-field measurements, as high-field stress can drive such devices into a regime with shifted CNP or even multiple CNPs (see Supporting Information). Thus, before and after each high electric field measurement, we performed a gate voltage sweep at low source–drain bias to locate the CNP (Figure 2a) and ensure that it had not shifted.

Current was normalized by device width (to yield current density I), and four-terminal voltage was normalized by center-to-center separation between voltage probes (to obtain the

DOI: 10.1021/acsnano.7b03878
ACS Nano 2017, 11, 9914–9919

lateral field F in the channel), as shown in Figure 2b. Due to the high mobility of our devices (see below), the current increases rapidly with electric field at low fields, and current saturation begins at fields much lower (~0.1 V/μm) than those in previous studies.[4,21] The largest current density measured here was ~1.7 mA/μm or 5.15 × 10^8 A/cm^2, higher than that in previous reports for graphene on hBN[8] (and much higher than typical Cu interconnects at ~10^7 A/cm^2) but limited by the lateral fields, which were kept moderate to avoid sample instability and breakdown.

We use current density to calculate drift velocity, $v_d = I/(en)$, where e is the elementary charge, $n \approx (C/e)(V_G - V_0 + V_{DS}/2)$ is the average carrier density,[4] and $C = 1.152 \times 10^{-8}$ F/cm^2 is the capacitance per unit area over the hBN and SiO_2 layers, as obtained from Hall and SdH measurements (Figure 1c). This approximation justifiably neglects the low residual density of carriers near the CNP[30] caused by charged impurities and thermal generation (see Supporting Information). Due to the low impurity density of hBN-encapsulated graphene,[31] thermal carrier generation dominates the uncertainty of the carrier density calculation, which is estimated to be <1% here for $|V_G| > 10$ V, even at RT.[4] The possible maximum error in v_d caused by the potential variation along the channel is estimated to be between 5 and 15%, depending on the carrier density (see Supporting Information).

As shown in Figure 3, the mobility $\mu = \sigma/(ne)$ extracted from the curves in Figure 2b is consistent with the value calculated

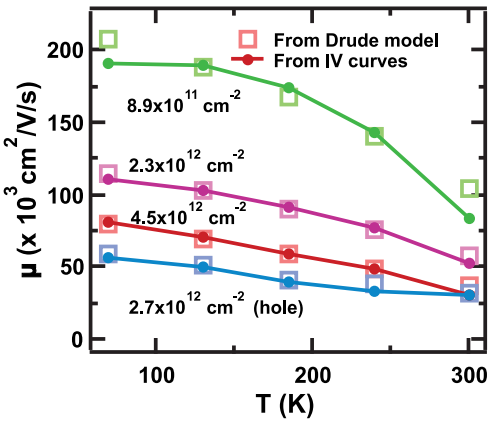

Figure 3. Temperature- and density-dependent mobility shows good correlation between estimates from linear fits to v_d *vs* $|F|$ curves at low field (lines) and from the Drude model (square symbols).

from the Drude model, where σ is the conductivity at zero magnetic field. Electron mobility increases with decreasing temperature, ranging from 80 × 10^3 cm^2/Vs at 300 K to 207 × 10^3 cm^2/Vs at 70 K, in both cases at a density of 0.8 × 10^{12} cm^{-2}. The mobility also increases with decreasing carrier density. Hole mobility is lower than electron mobility in all devices measured in this study (see Figures 2a and 3). With carrier densities between 0.8 and 1.4 × 10^{12} cm^{-2}, the RT mean free path ranges from 0.6 to 1.2 μm at low fields (see Supporting Information), always smaller than the geometry of our Hall bar. Further, the mean free path is much smaller at high fields, suggesting that throughout our room temperature measurements the sample is in or near the diffusive transport regime appropriate for extracting an average drift velocity.

Figure 4a displays the drift velocity as a function of lateral electric field at several carrier densities, showing that velocity

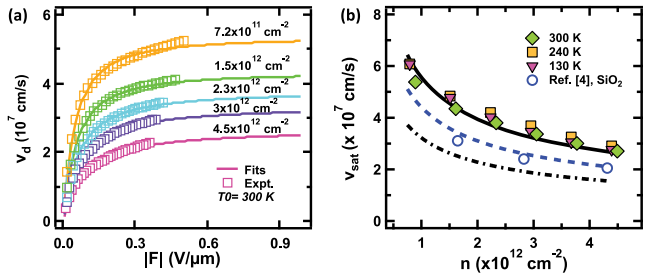

Figure 4. (a) Room temperature electron drift velocity *vs* field at several average carrier densities. Square symbols are experimental data; lines are fits to and extrapolations from eq 1. (b) Extracted saturation velocity *vs* electron density at various ambient temperatures. Color filled symbols are experimental data on hBN, whereas white filled circles are data from ref 4, v_{sat} of graphene on SiO_2. Lines are eq 3 with OP energies of 59 meV for SiO_2 (black dash-dotted line), 102 meV for hBN (black solid line), and 81 meV (blue dashed line) as an intermediate fit for graphene on SiO_2 as in ref 4.

does not fully saturate at the accessed fields, which were limited by device instability at higher fields. The slope of drift velocity *versus* lateral field at low field represents the device mobility, such that the steeper dependence of drift velocity on field in our device compared to that in samples of graphene on SiO_2[4] corresponds to the much higher low-field mobility of graphene encapsulated by hBN.

To extract saturation velocity v_{sat}, we fit drift velocity data in Figure 4a to the commonly used equation[4,21,32,33]

$$v_d(F) = \frac{\mu F}{\left[1 + \left(\frac{\mu F}{v_{sat}}\right)^{\gamma}\right]^{1/\gamma}} \quad (1)$$

where μ is the mobility and γ is a temperature-dependent fitting factor.[32] Qualitatively, γ tunes the "sharpness" of the turnover from the low-field linear to the high-field saturation regime. For each density and temperature, we fix μ based on the slope of low-field v_d *versus* F data, leaving v_{sat} and γ as free fitting parameters. When we fit γ and v_{sat} in eq 1 to the experimentally derived drift velocity *versus* field at each carrier density, the resulting $v_d(F)$ surprisingly undershoots the experimental drift velocity for high fields, as can be seen at $|F| > 0.3$ V/μm in Figure 4a. If heating were significant, the opposite would be expected because at high fields heating would lower experimental drift velocity relative to the predictions of eq 1. Ignoring this subtlety, and thus likely slightly underestimating v_{sat}, least-squares fitting yields $v_{sat}(n)$ (Figure 4b). The saturation velocity decreases with increasing carrier density, consistent with previous results.[4,8,23] γ is between 0.7 to 1.2 and displays both density and temperature dependence (see Supporting Information), in line with Thornber's prediction.[32]

Velocity saturation in graphene depends on carrier density, but the peak values measured here are higher than those in most other materials. At low carrier densities, v_{sat} measures ~6 × 10^7 cm/s. At a carrier density of 4 × 10^{12} cm^{-2}, $v_{sat} \approx 3 \times 10^7$ cm/s at 300 K. At similar densities in graphene on SiO_2, v_{sat} reaches only 2 × 10^7 cm/s.[4] For other commonly studied materials such as MoS_2, Si, and Ge, saturation velocities of only 0.27 × 10^7,[34] 10^7,[33] and 0.6 × 10^7 cm/s,[35] respectively, have been realized at RT, with little dependence on carrier density.

DOI: 10.1021/acsnano.7b03878
ACS Nano 2017, 11, 9914–9919

Only for InSb do measured v_{sat} values reach comparably high: up to 5×10^7 cm/s at 300 K and ~5.5×10^7 cm/s at 77 K.[36]

Several mechanisms can cause velocity saturation. At low fields, elastic scattering with charged impurities at the graphene−hBN interface can lower mobility and drift velocity.[37] However, charged impurities are expected to play a less significant role in limiting the velocity saturation at high fields,[4] especially in hBN-encapsulated graphene, which has a lower density of interfacial impurities. From low-field resistivity measurements, we estimate the impurity density n_{imp} in our device to be 4.54×10^{10} cm^{-2} (see Supporting Information), much lower than previously reported $n_{imp} \approx 8.86 \times 10^{11}$ cm^{-2} for graphene on SiO_2.[4] Further, our device mobilities continue to increase with reducing temperature down to 50 K (Figure 3), in contrast to the mobility in graphene on SiO_2, which is constant below 200 K and is dominated by impurity scattering.[38] This suggests that charged impurities are not the dominant scattering mechanism in hBN-encapsulated graphene except at temperatures below 50 K.

Therefore, scattering due to intrinsic (graphene) and remote (hBN) phonons, specifically surface OPs, is the most likely mechanism for limiting the saturation velocity in our samples. Such OPs are expected to limit saturation velocity in graphene due to their higher energy, which enables them to inelastically scatter and relax the energy of electrons much more efficiently than acoustic phonons (APs).[39] In addition, the deformation potentials for OP scattering are higher than those for AP scattering,[8,10] rendering the rate of OP emission stronger than that of AP emission. In atomically thin materials like graphene, scattering can occur with both the intrinsic phonons of graphene and the (dynamically screened[7,10]) surface OPs of the substrate. Typically, the lower-energy of these phonons, here the hBN phonons, limit the saturation velocity.

As charge carriers accelerate to high energies in high electric fields, an energy difference arises between "forward" populated and unpopulated states.[4,6] When this energy difference exceeds the OP energy $\hbar\omega_{OP}$, high-energy carriers can emit OPs, scattering inelastically back into the lower-energy states. At source−drain separation of 4 μm, even at fields below 0.1 V/μm, the total potential difference is high enough to allow emission of graphene or hBN surface OPs, so the field rather than the total potential is the important parameter. At high field, v_{sat} can be related to the OP frequency ω_{OP}:[4,40]

$$v_{sat} = \frac{2}{\pi}\frac{\omega_{OP}}{\sqrt{\pi n}}\sqrt{1 - \frac{\omega_{OP}^2}{4\pi n v_F^2}}\frac{1}{N_{OP} + 1} \quad (2)$$

The dependence of v_{sat} on temperature is related to the phonon occupation, $N_{OP} = 1/(\exp(\hbar\omega_{OP}/k_BT) - 1)$. At high carrier densities and neglecting self-heating, eq 2 can be simplified[4,24,40] to

$$v_{sat} \approx \frac{2}{\pi}\frac{\omega_{OP}}{\sqrt{\pi n}} \quad (3)$$

In Figure 4b, extracted v_{sat} values closely follow eq 3 with $\hbar\omega_{OP}$ corresponding to the lowest hBN surface OP energy of ~102 meV,[8] suggesting that the emission of remote OPs is the dominant high-field scattering mechanism in our devices. The significance of phonon scattering is further supported by device mobilities, which are consistent with theoretical calculations of remote phonon-limited mobility proposed by Ong and Fischetti.[7,41] Considering the temperature dependence of N_{OP} in eq 2, v_{sat} is predicted to change only 1.2% as the temperature changes from 100 to 300 K, given a phonon energy $\hbar\omega_{OP}$ = 102 meV. Indeed, our observed v_{sat} is almost completely insensitive to temperature, as shown in Figure 4b.

By comparison, we note that in ref 4 the experimental v_{sat} in SiO_2-supported graphene was best fit with a phonon energy of ~81 meV, which corresponds neither to the SiO_2 remote OP (~59 meV) nor to the graphene intrinsic OP (~160 meV). Thus, ref 4 surmised that v_{sat} in graphene on SiO_2 is limited by a *combination* of intrinsic and remote OPs, whereas here it appears that the v_{sat} in graphene encapsulated by hBN is primarily limited by the hBN surface OPs. Naturally, more sophisticated simulations (beyond the scope of this work) are needed to confirm these observations, but the simple model present here appears to capture the limiting transport physics.

We do not observe complete velocity saturation nor the negative differential velocity (NDV) predicted in some theoretical models.[10,42] The saturation model of Serov *et al.*[10] predicted the appearance of NDV at high fields but only in the case of strong self-heating and at higher fields than are achievable in this work. As stated earlier, our measurements are limited by the requirement to keep samples stable and measurements repeatable during long high-field stress times. We estimate the maximum device temperature increase achieved in this work in Figure 5, considering the thermal

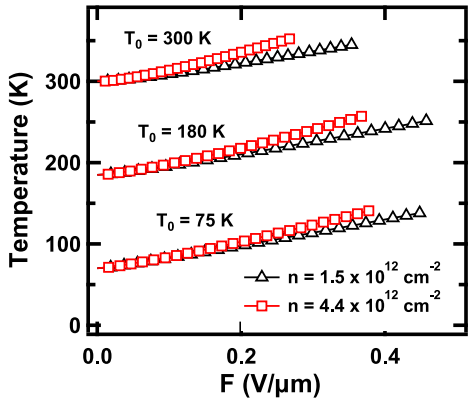

Figure 5. Modeled lattice temperature based on power input at different starting temperatures and carrier densities. T_0 is the substrate temperature, as listed for each estimate.

resistance of the hBN substrate, SiO_2 layer, and Si back gate (details provided in the Supporting Information). The maximum temperature increase is about 70 K in our measurements, insufficient to significantly increase the occupation of the high-energy hBN surface OPs. Thus, the lack of observed high-field NDV in our work is not unexpected; NDV could still occur at higher fields or carrier densities than are probed in this work.

The higher saturation velocity observed in our graphene samples encapsulated by hBN occurs due to a combination of factors. First, the higher-energy surface OPs of hBN compared to that of other substrates leads to a delayed onset of OP emission. Second, the mobility is higher in our samples than has been previously achieved or simulated in high-field studies (*e.g.*, in ref 10) due to lower impurity density. Third, our samples achieve saturation velocity at lower fields (and thus lower power) than was previously possible (*e.g.*, ~0.2 V/μm in Figure 4a *versus* ~1 V/μm in ref 4), as a consequence of the higher mobility. The lower power leads to less heating in these samples, as shown in Figure 5, with only ~70 K temperature

DOI: 10.1021/acsnano.7b03878
ACS Nano 2017, 11, 9914−9919

increase *versus* ~200 K temperature increase estimated in ref 4 for samples on SiO_2.

CONCLUSIONS

We have investigated high-field electric transport behavior in high-mobility graphene encapsulated by hBN. The excellent physical properties of hBN enable us to achieve the highest saturation velocities to date in graphene supported by insulating substrates, a critical property for electronic device applications. We conclude that in graphene encapsulated by hBN, the high-energy hBN surface phonons play an important role in ultimately limiting carrier drift velocity, whereas impurity scattering and lattice heating are less significant. These results suggest that further investigation of high-field behavior in graphene may enable high-electric-field graphene devices with remarkable properties.

METHODS

Devices were fabricated through mechanical exfoliation of highly ordered pyrolytic graphite and hexagonal boron nitride crystals, followed by van der Waals stacking with poly(propylene carbonate)/poly(methyl methacrylate) stamps[26] onto a 300 nm SiO_2 substrate over a heavily (n++) doped Si global back gate, creating a sandwich of monolayer graphene between two hBN films 32−55 nm thick (see Supporting Information). The heterostructures were annealed[43] at 500 °C in flowing O_2/Ar (50/5 sccm) for 1 h to remove residues introduced by the transfer process. The devices were then patterned into a Hall bar geometry with a center-to-center voltage probe distance of 4 μm and a width of 2 μm (Figure 1a), using electron beam lithography followed by a dry etch. Low-resistance ohmic edge contacts were made by depositing Cr/Au with electron beam evaporation.[44]

Magnetoresistances were measured with standard lock-in technique in a He vapor variable-temperature insert cryostat with a base temperature of 1.6 K and magnetic fields up to 14 T. High lateral electric field transport measurements were performed in vacuum or ^{4}He vapor at temperatures between 10 and 300 K using a Keithley 2400 as the voltage source and an Agilent 34401 Digital Multimeter for measuring the voltage drop locally across the device.

ASSOCIATED CONTENT

Supporting Information

The Supporting Information is available free of charge on the ACS Publications website at DOI: 10.1021/acsnano.7b03878.

Further device details, discussion of device instabilities, v_{sat} extraction error estimation, impurity density calculations, mean free path calculation, discussion of v_{sat} extraction parameter, temperature simulation details, and sequence dependence of I−V measurements (PDF)

AUTHOR INFORMATION

Corresponding Author

*E-mail: goldhaber-gordon@stanford.edu.

ORCID

Eric Pop: 0000-0003-0436-8534

Author Contributions

M.Y. began the work and designed the research strategy. M.Y. synthesized encapsulated graphene samples, and W.Y. performed device design, AFM characterization, and electron beam lithography. W.Y. and M.Y. carried out data analysis, while W.Y. produced figures. D.G.G. and E.P. facilitated interpretation of results, with E.P. providing methods for temperature modeling. All authors discussed the results and revised the paper.

Notes

The authors declare no competing financial interest.

ACKNOWLEDGMENTS

The authors thank Menyoung Lee for vital insight and support during the first half of the project, and Trevor Petach for guidance on measurement setup. Work was primarily funded by the Air Force Office of Scientific Research, Award Nos. FA9550-14-1-0251 and FA9550-16-1-0126, with additional support from the National Science Foundation EFRI 2-DARE Grant 1542883, and from the Gordon and Betty Moore Foundation through Grant No. GBMF3429. Work was performed in part at the Stanford Nano Shared Facilities (SNSF), supported by the National Science Foundation under award ECCS-1542152. W.Y. is grateful for a scholarship provided by China Scholarship Council (No. 201504910559).

REFERENCES

(1) Geim, A. K.; Novoselov, K. S. The Rise of Graphene. *Nat. Mater.* **2007**, *6*, 183−191.

(2) Katsnelson, M. I. *Graphene: Carbon in Two Dimensions.* **2012**, 1−351.

(3) Chen, J. H.; Jang, C.; Adam, S.; Fuhrer, M. S.; Williams, E. D.; Ishigami, M. Charged-Impurity Scattering in Graphene. *Nat. Phys.* **2008**, *4*, 377−381.

(4) Dorgan, V. E.; Bae, M. H.; Pop, E. Mobility and Saturation Velocity in Graphene on Sio2. *Appl. Phys. Lett.* **2010**, *97*, 082112.

(5) Dorgan, V. E.; Behnam, A.; Conley, H. J.; Bolotin, K. I.; Pop, E. High-Field Electrical and Thermal Transport in Suspended Graphene. *Nano Lett.* **2013**, *13*, 4581−4586.

(6) Fang, T.; Konar, A.; Xing, H. L.; Jena, D. High-Field Transport in Two-Dimensional Graphene. *Phys. Rev. B: Condens. Matter Mater. Phys.* **2011**, *84*, 125450.

(7) Ong, Z. Y.; Fischetti, M. V. Theory of Interfacial Plasmon-Phonon Scattering in Supported Graphene. *Phys. Rev. B: Condens. Matter Mater. Phys.* **2012**, *86*, 165422.

(8) Perebeinos, V.; Avouris, P. Inelastic Scattering and Current Saturation in Graphene. *Phys. Rev. B: Condens. Matter Mater. Phys.* **2010**, *81*, 195442.

(9) Pop, E.; Varshney, V.; Roy, A. K. Thermal Properties of Graphene: Fundamentals and Applications. *MRS Bull.* **2012**, *37*, 1273−1281.

(10) Serov, A. Y.; Ong, Z. Y.; Fischetti, M. V.; Pop, E. Theoretical Analysis of High-Field Transport in Graphene on a Substrate. *J. Appl. Phys.* **2014**, *116*, 034507.

(11) Castro Neto, A. H.; Guinea, F.; Peres, N. M. R.; Novoselov, K. S.; Geim, A. K. The Electronic Properties of Graphene. *Rev. Mod. Phys.* **2009**, *81*, 109−162.

(12) Bolotin, K. I.; Sikes, K. J.; Jiang, Z.; Klima, M.; Fudenberg, G.; Hone, J.; Kim, P.; Stormer, H. L. Ultrahigh Electron Mobility in Suspended Graphene. *Solid State Commun.* **2008**, *146*, 351−355.

(13) Balandin, A. A. Thermal Properties of Graphene and Nanostructured Carbon Materials. *Nat. Mater.* **2011**, *10*, 569−581.

(14) Yu, J.; Liu, G. X.; Sumant, A. V.; Goyal, V.; Balandin, A. A. Graphene-on-Diamond Devices with Increased Current-Carrying Capacity: Carbon Sp(2)-on-Sp(3) Technology. *Nano Lett.* **2012**, *12*, 1603−1608.

(15) Young, A. F.; Kim, P. Quantum Interference and Klein Tunnelling in Graphene Heterojunctions. *Nat. Phys.* **2009**, *5*, 222−226.

(16) Novoselov, K. S.; Geim, A. K.; Morozov, S. V.; Jiang, D.; Katsnelson, M. I.; Grigorieva, I. V.; Dubonos, S. V.; Firsov, A. A. Two-Dimensional Gas of Massless Dirac Fermions in Graphene. *Nature* **2005**, *438*, 197−200.

DOI: 10.1021/acsnano.7b03878
ACS Nano 2017, 11, 9914−9919

(17) Yu, P. Y.; Cardona, M. *Fundamentals of Semiconductors: Physics and Materials Properties*, 4th ed.; Springer: Berlin, 2010; pp 1−775.
(18) Sze, S. M.; Ng, K. K. *Physics of Semiconductor Devices*, 3rd ed.; Wiley-Interscience: Hoboken, NJ, 2007.
(19) Han, S. J.; Garcia, A. V.; Oida, S.; Jenkins, K. A.; Haensch, W. Graphene Radio Frequency Receiver Integrated Circuit. *Nat. Commun.* **2014**, *5*, 3086.
(20) Behnam, A.; Lyons, A. S.; Bae, M. H.; Chow, E. K.; Islam, S.; Neumann, C. M.; Pop, E. Transport in Nanoribbon Interconnects Obtained from Graphene Grown by Chemical Vapor Deposition. *Nano Lett.* **2012**, *12*, 4424−4430.
(21) Ramamoorthy, H.; Somphonsane, R.; Radice, J.; He, G.; Kwan, C. P.; Bird, J. P. "Freeing" Graphene from Its Substrate: Observing Intrinsic Velocity Saturation with Rapid Electrical Pulsing. *Nano Lett.* **2016**, *16*, 399−403.
(22) Fischetti, M. V.; Kim, J.; Narayanan, S.; Ong, Z. Y.; Sachs, C.; Ferry, D. K.; Aboud, S. J. Pseudopotential-Based Studies of Electron Transport in Graphene and Graphene Nanoribbons. *J. Phys.: Condens. Matter* **2013**, *25*, 473202.
(23) Meric, I.; Dean, C.; Young, A.; Hone, J.; Kim, P.; Shepard, K. L. Graphene Field-Effect Transistors Based on Boron Nitride Gate Dielectrics. *IEEE Int. Electron Devices Meeting (IEDM)* **2010**, 23.2.1.
(24) Meric, I.; Han, M. Y.; Young, A. F.; Ozyilmaz, B.; Kim, P.; Shepard, K. L. Current Saturation in Zero-Bandgap, Topgated Graphene Field-Effect Transistors. *Nat. Nanotechnol.* **2008**, *3*, 654−659.
(25) Sichel, E. K.; Miller, R. E.; Abrahams, M. S.; Buiocchi, C. J. Heat-Capacity and Thermal-Conductivity of Hexagonal Pyrolytic Boron-Nitride. *Phys. Rev. B* **1976**, *13*, 4607−4611.
(26) Dean, C. R.; Young, A. F.; Meric, I.; Lee, C.; Wang, L.; Sorgenfrei, S.; Watanabe, K.; Taniguchi, T.; Kim, P.; Shepard, K. L.; Hone, J. Boron Nitride Substrates for High-Quality Graphene Electronics. *Nat. Nanotechnol.* **2010**, *5*, 722−726.
(27) Hwang, C.; Siegel, D. A.; Mo, S. K.; Regan, W.; Ismach, A.; Zhang, Y. G.; Zettl, A.; Lanzara, A. Fermi Velocity Engineering in Graphene by Substrate Modification. *Sci. Rep.* **2012**, *2*, 590.
(28) Zhang, Y. B.; Tan, Y. W.; Stormer, H. L.; Kim, P. Experimental Observation of the Quantum Hall Effect and Berry's Phase in Graphene. *Nature* **2005**, *438*, 201−204.
(29) Novoselov, K. S.; Jiang, Z.; Zhang, Y.; Morozov, S. V.; Stormer, H. L.; Zeitler, U.; Maan, J. C.; Boebinger, G. S.; Kim, P.; Geim, A. K. Room-Temperature Quantum Hall Effect in Graphene. *Science* **2007**, *315*, 1379−1379.
(30) Nagashio, K.; Nishimura, T.; Toriumi, A. Estimation of Residual Carrier Density near the Dirac Point in Graphene through Quantum Capacitance Measurement. *Appl. Phys. Lett.* **2013**, *102*, 173507.
(31) Banszerus, L.; Schmitz, M.; Engels, S.; Dauber, J.; Oellers, M.; Haupt, F.; Watanabe, K.; Taniguchi, T.; Beschoten, B.; Stampfer, C. Ultrahigh-Mobility Graphene Devices from Chemical Vapor Deposition on Reusable Copper. *Science Advances* **2015**, *1*, e1500222.
(32) Thornber, K. K. Relation of Drift Velocity to Low-Field Mobility and High-Field Saturation Velocity. *J. Appl. Phys.* **1980**, *51*, 2127−2136.
(33) Caughey, D. M.; Thomas, R. E. Carrier Mobilities in Silicon Empirically Related to Doping and Field. *Proc. IEEE* **1967**, *55*, 2192−3.
(34) Fiori, G.; Szafranek, B. N.; Iannaccone, G.; Neumaier, D. Velocity Saturation in Few-Layer Mos2 Transistor. *Appl. Phys. Lett.* **2013**, *103*, 233509.
(35) Jacoboni, C.; Nava, F.; Canali, C.; Ottaviani, G. Electron-Drift Velocity and Diffusivity in Germanium. *Phys. Rev. B: Condens. Matter Mater. Phys.* **1981**, *24*, 1014−1026.
(36) Neukermans, A.; Kino, G. S. Absolute Measurement of Electron Velocity-Field Characteristic of Insb. *Phys. Rev. B* **1973**, *7*, 2703−2709.
(37) Ong, Z. Y.; Fischetti, M. V. Charged Impurity Scattering in Top-Gated Graphene Nanostructures. *Phys. Rev. B: Condens. Matter Mater. Phys.* **2012**, *86*, 121409.
(38) Chen, J. H.; Jang, C.; Xiao, S. D.; Ishigami, M.; Fuhrer, M. S. Intrinsic and Extrinsic Performance Limits of Graphene Devices on Sio2. *Nat. Nanotechnol.* **2008**, *3*, 206−209.
(39) Lundstrom, M. *Fundamentals of Carrier Transport*, 2nd ed.; Cambridge University Press: London, 2009.
(40) Li, Z.; Dorgan, V. E.; Serov, A.; Pop, E. High-Field and Thermal Transport in Graphene. In *2D Materials for Nanoelectronics*; Houssa, M., Dimoulas, A., Molle, A., Eds.; Taylor & Francis Group, LLC: Boca Raton, FL, 2016; pp 107−138.
(41) Ong, Z. Y.; Fischetti, M. V. Theory of Remote Phonon Scattering in Top-Gated Single-Layer Graphene. *Phys. Rev. B: Condens. Matter Mater. Phys.* **2013**, *88*, 045405.
(42) Shishir, R. S.; Ferry, D. K. Velocity Saturation in Intrinsic Graphene. *J. Phys.: Condens. Matter* **2009**, *21*, 344201.
(43) Garcia, A. G. F.; Neumann, M.; Amet, F.; Williams, J. R.; Watanabe, K.; Taniguchi, T.; Goldhaber-Gordon, D. Effective Cleaning of Hexagonal Boron Nitride for Graphene Devices. *Nano Lett.* **2012**, *12*, 4449−4454.
(44) Wang, L.; Meric, I.; Huang, P. Y.; Gao, Q.; Gao, Y.; Tran, H.; Taniguchi, T.; Watanabe, K.; Campos, L. M.; Muller, D. A.; Guo, J.; Kim, P.; Hone, J.; Shepard, K. L.; Dean, C. R. One-Dimensional Electrical Contact to a Two-Dimensional Material. *Science* **2013**, *342*, 614−617.

NOTE ADDED AFTER ASAP PUBLICATION

This paper was published ASAP on September 14, 2017 with errors in Figures 3, 4, and 5. The corrected version was posted on September 18, 2017.

DOI: 10.1021/acsnano.7b03878
ACS Nano 2017, 11, 9914−9919

Supporting Information

High Velocity Saturation in Graphene Encapsulated by Hexagonal Boron Nitride

*Megan A. Yamoah[1,2,†], Wenmin Yang[1,3], Eric Pop[4,5,6], David Goldhaber-Gordon[1]**

[1]Department of Physics, Stanford University, Stanford, CA 94305, USA

[2]Department of Physics, Massachusetts Institute of Technology, Cambridge, MA 02139, USA

[3]Beijing National Laboratory for Condensed Matter Physics, Institute of Physics, Chinese Academy of Sciences, Beijing 100190, China

[4] Department of Electrical Engineering, Stanford University, Stanford, CA 94305, USA

[5]Department of Materials Science & Engineering, Stanford University, Stanford, CA 94305, USA

[6]Precourt Institute for Energy, Stanford University, Stanford, CA 94305, USA

*E-mail: goldhaber-gordon@stanford.edu

[†]Present Address: Department of Physics, Massachusetts Institute of Technology, 77 Massachusetts Avenue, Cambridge, MA 02139, USA

1. Further device details: The device presented had a bottom hBN thickness of 32 nm and top hBN thickness of 55 nm. Etched areas leave less than 5 nm of the bottom hBN layer. Edge contacts were deposited by electron beam evaporation of 3 nm Cr followed by 110 nm Au. An optical image of the device is shown in Figure S1.

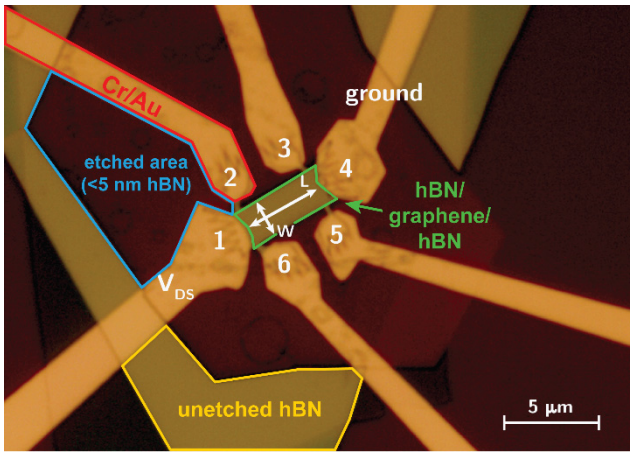

Figure S1. Optical image of main fabricated device with contacts numbers as in main text Figure 1. The zigzag outline of the Cr/Au edge contacts can be seen in the figure. Regions of differing material composition are shown by the colored outlines.

2. Graphene thickness: Our graphene samples are exfoliated on n++ Si wafers with 300 nm thick SiO_2, and only monolayer graphene flakes are selected for measurements. We determine these graphene flakes optically with white light illumination as performed by several groups and discussed in Ref. 1. In Figures S2 and S3, we show representative examples of exfoliated graphene and graphite with monolayer, bilayer, and multilayer flakes with corresponding color histograms for selected regions marked by red ovals in the optical image. In Ref. 1, determination of graphene thickness by optical contrast is analyzed for substrates with 300 nm and 200 nm SiO_2. Contrast on 300 nm SiO_2 is improved under green light as reported by Ref. 1 and as visible in our histogram, which is better-separated in the green channel. However, we can effectively determine graphene thickness by eye even under white light. Each chip from which we chose monolayer graphene

samples for our devices contained mono-, bi-, and multilayer samples, allowing comparison of contrast under consistent external lighting.

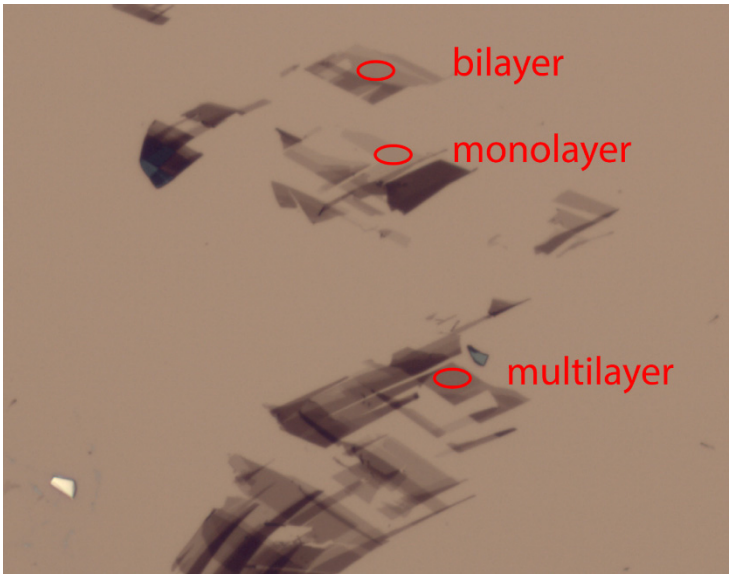

Figure S2. Optical image of typical exfoliated graphene flakes on a 300 nm SiO_2 on Si wafer with mono-, bi-, and multilayer samples. Red ovals denote selection samples used in Figure S3.

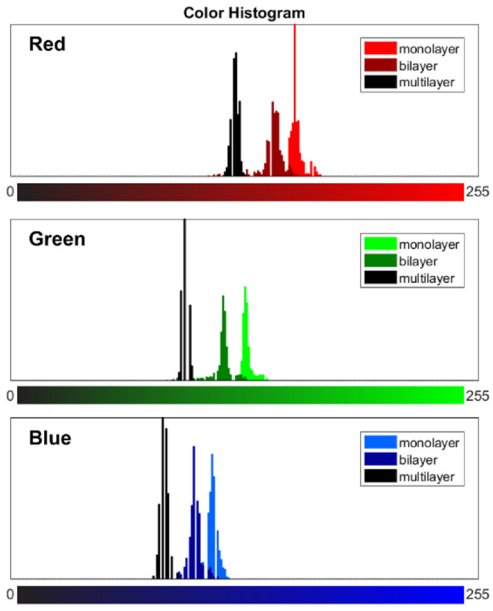

Figure S3. Color histogram comparing pixel color counts for mono-, bi-, and multilayer flakes from selection samples shown in Figure S2.

3. Device instability: In nearly all the 14 measured hBN-encapsulated graphene samples, measuring at high biases and high carrier densities induced device instability. After high-bias measurements, the Charge Neutrality Point (CNP) would shift and/or multiple resistance peaks would appear, as seen in Figure S4. During I-V measurements, such shifts were evidenced by a sudden drop in current as bias was increased, indicating an abrupt increase in device resistivity. One possible explanation is creation of charge traps at or near the graphene-hBN substrate interface[2] during high-field stress. Understanding this phenomenon will require additional experimental and theoretical effort. Apart from that shown in Figure S4, all data presented in this study are taken from measurements on devices *not* pushed into the unstable regime, as determined by an unchanging CNP before and after I-V measurements.

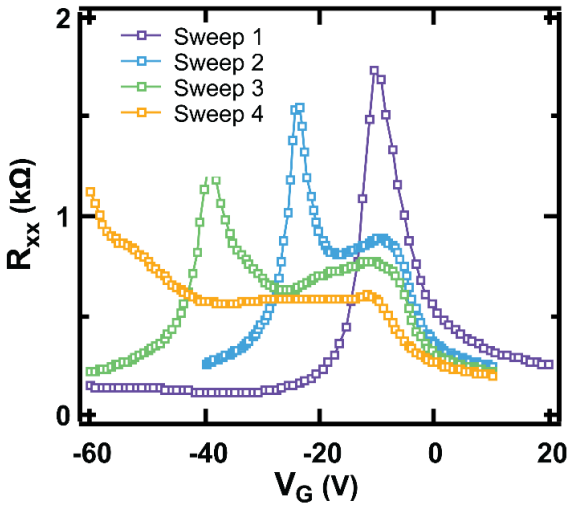

Figure S4. Unstable, changing CNP after successive high-field stress measurements.

4. Sources of error: To estimate the drift velocity from the measured current, we assumed spatially uniform carrier density within the Hall bar, as $n \approx (C/e)(V_{\mathrm{G}} - V_0 + V_{\mathrm{DS}}/2)$. However, at high lateral field from bias V_{DS}, there may be deviations from this approximation which could be a source of error in calculating the drift velocity $v_{\mathrm{d}} = I/(en)$ and saturation velocity v_{sat} (where I is the current per width). Specifically, at the lowest carrier density probed, the maximum

V_{DS} is 15% of V_G and could contribute to a variation in v_d. Calculating v_{sat} in two limits enables us to quantify this error. First, assuming no effect of bias voltage V_{DS} on effective gate voltage (a correct description near the source), we take $n = (C/e)(V_G - V_0)$, giving an upper limit on drift velocity, $v_{sat_{max}}$. Then, assuming the maximum effect of V_{DS} (a correct description near the drain), we take $n = (C/e)(V_G - V_0 + V_{DS})$ and find a lower limit, $v_{sat_{min}}$. Our average relative error $\varepsilon = \frac{v_{sat_{max}} - v_{sat_{min}}}{v_{sat}}$ in the extraction of saturation velocity is then ±15% at low densities, and down to ±5% at the highest densities measured. In Figure S5, the relative error calculated in this way is presented for data taken at room temperature (RT).

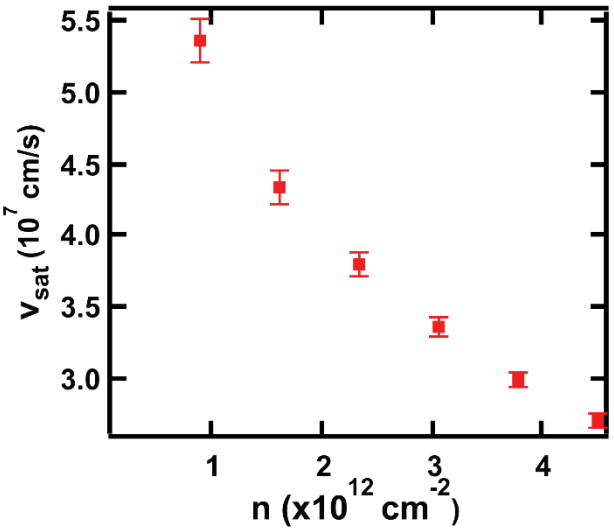

Figure S5. Calculated error in v_{sat} for RT data

5. Impurity density calculation: We estimate impurity density with the method discussed in Ref. 3 and replicated in Ref. 4. Impurity density $n_{imp} = BC|d\sigma/dV_G|^{-1}$ where $B = 5 \times 10^{15}$ $V^{-1}s^{-1}$ is a constant produced by the screened Coulomb potential in the random phase approximation,[5] and the measured capacitance $C = 1.152 \times 10^{-8}$ F/cm^2. As shown in Figure S6, we fit to RT low-field σ vs. V_G data over a 2 V interval centered at $V_G = 2$ V to extract $d\sigma/dV_G = 1.26 \times 10^3$ (S/V) and $n_{imp} = 4.54$ x 10^{10} cm^{-2}. We further obtain the surface potential variation $\Delta \approx \hbar v_F(\pi n^*)^{1/2} = 13.5$

meV, where $n^* = 0.279\ n_{imp}$ is the residual carrier puddle density.[6] Comparing to $\Delta = 59$ meV for graphene on SiO_2 (Ref. 4), we find that our hBN-encapsulated graphene devices exhibit lower impurity density due to the cleaner graphene interfaces. We find the thermally generated carrier density by[4] $n_{th} = (\pi/2)(k_B T/v_F h)^2$. At RT, we find $n_{th} = 8.03 \times 10^{10}$ cm^{-2} in our sample.

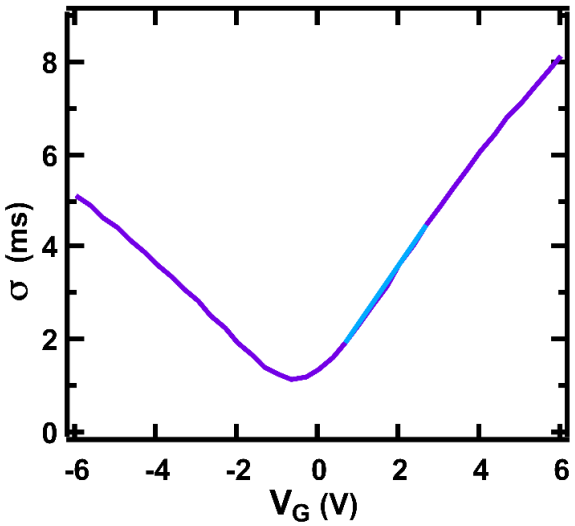

Figure S6. Linear fit (blue) at $V_G = 2$ V to extract $d\sigma/dV_G$ for at room temperature (RT).

6. Mean free path calculation: We first estimate the *low-field* mean free path of charge carriers in our device. With $l = v_f \tau$ and $\sigma = e^2 \tau \frac{v_f}{\hbar \pi} k_f$, we have $l = (\hbar/e)\mu\sqrt{n\pi}$.[7] At RT, the mean free path ranges from 0.6 to 2 μm at a carrier density of 0.8 to 1.4 × 10^{12} cm^{-2}. At 10 K, we have $l =$ 1.6 to $l = 2.3$ μm. We note that at *high-field* (in velocity saturation) the mean free paths are about an order of magnitude lower (see e.g. momentum loss rates calculated in Ref. 10 of the main text, depending on field and temperature), ensuring that our samples are in the diffusive transport regime when v_{sat} is extracted.

7. Fitting parameter γ: As stated in the main text, in our v_{sat} extraction, the dimensionless free fitting parameter γ affects the "sharpness" of the turnover from the low-field linear to the high-field saturation regime and is possibly related to low-field mobility. As shown in Figure S7, γ

displays both temperature and carrier density dependence but remains within a fairly narrow range between 0.7 and 1.2.

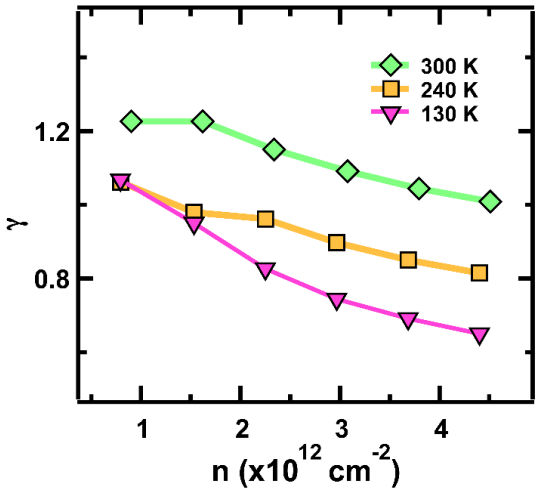

Figure S7. Fitting parameter γ dependence on both carrier density and temperature

8. Device temperature simulations: We take our temperature modeling scheme from Ref. 4. Based on extensive finite-element simulations in Ref. 8, reproduced in Ref. 4, we take the temperature of graphene to be constant across the device. The average graphene lattice temperature is estimated as $\Delta T = T - T_0 = P(R_{BN} + R_{ox} + R_{Si})$ when $W, L \gg t_{ox}$. Here t_{ox} is the oxide thickness, T_0 is the ambient temperature, and P is the electrical (Joule) power input. The thermal resistance of the hBN layer is $R_{BN} = t_{BN} / (k_{BN}WL)$, where k_{BN} is the cross-plane thermal conductivity of hBN at RT and t_{BN} is the layer thickness.[9] The temperature dependence of the SiO_2 and Si thermal conductivity are taken into account following Dorgan *et al*.[4] Thus, since R_{ox} and R_{Si} depend on temperature, ΔT is calculated iteratively (in Figure 5 of main text) until the total thermal resistance changes by less than 0.3% from one step to the next.

9. Dependence of v_{sat} on measurement sequence: As presented in the main text, we found that the v_{sat} is relatively insensitive to ambient temperature. However, the highest values were obtained from the first measurement sequence on each device. These results were discarded for the analysis presented in the main text. Instead, we analyzed data from subsequent measurements with lower, but repeatable v_{sat} values, regardless of temperature. Figure S8 shows v_{sat} vs. n data taken at RT, at different points in the measurement sequence. The first I-V measurement (Sequence 1) performed at RT resulted in the highest v_{sat}. After cooling the sample, extracted v_{sat} values are lower than the initial RT data. We then re-measured the sample at RT twice (Sequences 2 and 3), obtaining v_{sat} values comparable to each other and comparable to values extracted from the low temperature data. While we did not extensively study this phenomenon, we predict that the first measurement permanently populates certain charge traps in the device, leading to consistent carrier transport in subsequent measurements.

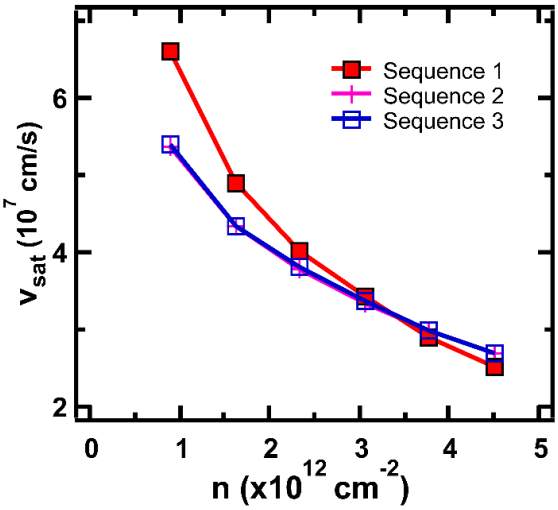

Figure S8. v_{sat} dependence on measurement order

10. Data from another device: Figure S9 presents v_{sat} vs. n data from a second device of length 4 μm and width 2 μm, in addition to that presented in the main text. This device also displays

saturation consistent with the hBN surface optical phonon energy of ~102 meV (or slightly higher) as given by Eq. (3) in the main text: $v_{sat} = \frac{2}{\pi}\frac{\omega_{OP}}{\sqrt{\pi n}}$.

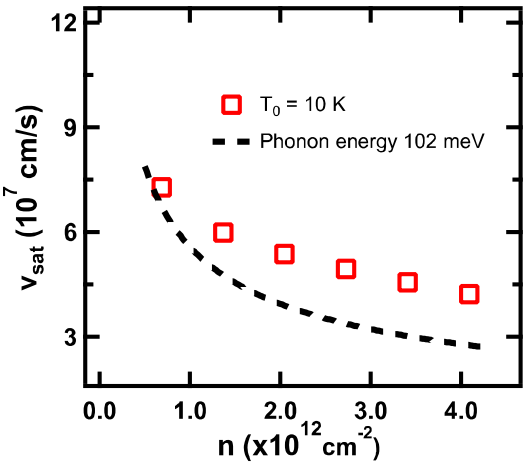

Figure S9. Extracted v_{sat} vs. electron carrier density for a second device taken at an ambient device temperature of 10 K. The dotted line is the simple fit using Eq. (3) in the main text, with $\hbar\omega_{OP} \approx$ 102 meV, the lowest energy of hBN surface optical phonons.

Supplementary References:

1. Blake, P.; Hill, E. W.; Castro Neto, A. H.; Novoselov, K. S.; Jiang, D.; Yang, R.; Booth, T. J.; Geim, A. K., Making Graphene Visible. *Appl Phys Lett* **2007,** *91*, 063124.
2. Wong, D.; Velasco, J.; Ju, L.; Lee, J.; Kahn, S.; Tsai, H. Z.; Germany, C.; Taniguchi, T.; Watanabe, K.; Zettl, A.; Wang, F.; Crommie, M. F., Characterization and Manipulation of Individual Defects in Insulating Hexagonal Boron Nitride Using Scanning Tunnelling Microscopy. *Nat Nanotechnol* **2015,** *10*, 949–953.
3. Chen, J. H.; Jang, C.; Adam, S.; Fuhrer, M. S.; Williams, E. D.; Ishigami, M., Charged-Impurity Scattering in Graphene. *Nat Phys* **2008,** *4*, 377-381.
4. Dorgan, V. E.; Bae, M. H.; Pop, E., Mobility and Saturation Velocity in Graphene on Sio2. *Appl Phys Lett* **2010,** *97*, 082112.
5. Hwang, E. H.; Adam, S.; Das Sarma, S., Carrier Transport in Two-Dimensional Graphene Layers. *Phys Rev Lett* **2007,** *98*, 186806.
6. Adam, S.; Hwang, E. H.; Galitski, V. M.; Das Sarma, S., A Self-Consistent Theory for Graphene Transport. *P Natl Acad Sci USA* **2007,** *104*, 18392-18397.
7. Das Sarma, S.; Adam, S.; Hwang, E. H.; Rossi, E., Electronic Transport in Two-Dimensional Graphene. *Rev Mod Phys* **2011,** *83*, 407-470.
8. Bae, M. H.; Ong, Z. Y.; Estrada, D.; Pop, E., Imaging, Simulation, and Electrostatic Control of Power Dissipation in Graphene Devices. *Nano Lett* **2010,** *10*, 4787-4793.
9. Sichel, E. K.; Miller, R. E.; Abrahams, M. S.; Buiocchi, C. J., Heat-Capacity and Thermal-Conductivity of Hexagonal Pyrolytic Boron-Nitride. *Phys Rev B* **1976,** *13*, 4607-4611.